Dalton Transactions

ROYAL SOCIETY OF CHEMISTRY

PAPER

View Article Online
View Journal | View Issue

Cite this: *Dalton Trans.*, 2025, **54**, 7874

Metal ion independent conductance through bis-chelated metal complex molecular wires based on a bis(diphenylphosphino)aniline derivative†

Marco F. Gatto,‡[a] Sara Sangtarash,*‡[b] David Jago,[c] R. Tom Abram,[a] Eleanor Barrett,[a] Amit Sil,[a] George A. Koutsantonis,[c] Simon J. Higgins,[a] Craig M. Robertson,[a] Richard J. Nichols,[a] Hatef Sadeghi*[b] and Andrea Vezzoli*[a]

Received 5th February 2025,
Accepted 1st April 2025

DOI: 10.1039/d5dt00292c

rsc.li/dalton

It is becoming increasingly evident that transition metal complexes impart desirable qualities in single-molecule electronics, and testing metallic centres in combination with appropriate ligands is salient to building the next generation of single-molecule devices. Metal-phosphine complexes have been the subject of very few studies, despite their extensive use in other areas of chemistry. In this contribution, we fabricated and studied robust single-molecule junctions using linear bis-chelated ligand–metal–ligand complexes of the type $[M(PNP)_2]PF_6$ (M = Cu(I), Ag(I) or Au(I); PNP = bis(diphenylphosphino)aniline functionalised with methylthio contact groups). The robustness of the devices was evinced by surface-enhanced Raman spectroscopy (SERS) and scanning-tunnelling microscopy break junction (STM-BJ) methods, and the conductance of the devices was found to be independent of the central transition metal. Quantum transport calculations show consistent HOMO–LUMO gaps between the studied complexes in the transmission plots, supporting the experimental findings. This study shows that bis-chelation is a viable approach to the fabrication of stable and robust metal-phosphine devices.

Introduction

Metal complexes offer a wide degree of freedom in the design of molecular wires for nanoelectronics applications.[1] In addition to tailoring the final charge transport behaviour of the resulting single-molecule junction (Fig. 1a) by choosing appropriate ligands, the metallic centre can be used, for instance, to impart electrochemical response by exploiting their multiple redox states,[2,3] to grant long-range coherent transport by leveraging metal–metal bonds,[4,5] and even to induce mechanosensitivity through spin-crossover[6] or quantum interference[7] phenomena. The ligand–metal interface is a key factor in ensuring both high electrical conductance and coherent mechanisms of charge transport. Covalent interfaces, such as those observed in bis(acetylide) organometallic species,[8] have demonstrated efficient charge transport and low conductance attenuation with length, ensuring phase-

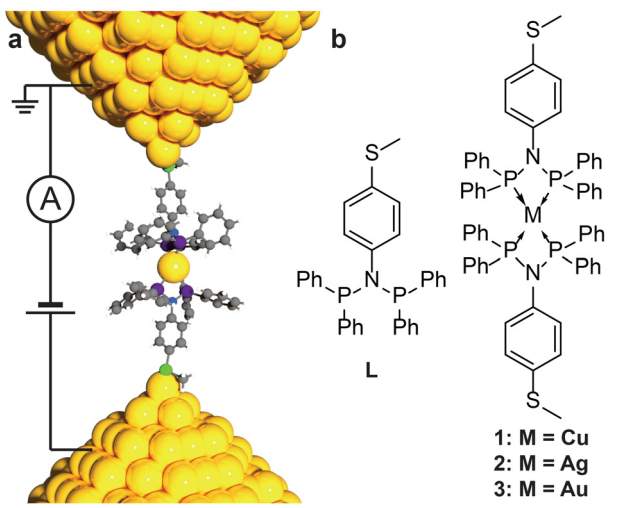

Fig. 1 (a) Idealised structure of a single-molecule junction, with the molecule sandwiched between two metallic electrodes. (b) Structures of the compounds used in this study. Colour legend in (a): C = grey, H = white, N = blue, P = purple, S = green, Au = yellow.

[a]*Department of Chemistry, University of Liverpool, Crown Street, Liverpool L69 7ZD, UK. E-mail: andrea.vezzoli@liverpool.ac.uk*
[b]*Device Modelling Group, School of Engineering, University of Warwick, Coventry CV4 7AL, UK. E-mail: hatef.sadeghi@warwick.ac.uk, sara.sangtarash@warwick.ac.uk*
[c]*School of Molecular Sciences, University of Western Australia, Perth, Western Australia 6009, Australia*

†Electronic supplementary information (ESI) available. CCDC 2408349–2408351. For ESI and crystallographic data in CIF or other electronic format see DOI: https://doi.org/10.1039/d5dt00292c

‡These authors contributed equally to this work

coherent mechanisms over long tunnelling distances.[9] On the other hand, coordinative interfaces (*e.g.* pyridyl-metal, metallocenes, *etc.*) have been shown in many cases to be not as electronically transparent, impairing charge transport and in extreme cases even causing phase decoherence as a result of a change to "hopping-like" mechanisms of charge transport,[10,11] with multiple sequential tunnelling steps and charge residing on the redox-active metal centres a finite time.

Of all the coordination complexes available, pyridyl and poly(pyridyl) systems are amongst the most studied. Bidentate 2,2′-dipyridyl[12–15] and tridentate 2,2′;6′,2″-terpyridyl-based complexes[16–19] have been widely explored due to their stability and ease of synthesis. Carboxylate-based complexes also feature in the literature, as a prominent example of a hard ligand used in molecular electronics.[20,21] Much less studied are phosphine-metal complexes, in spite of their relevance in coordination chemistry for applications in catalysis, their electronic structure that grants σ-bonding behaviour while allowing back-bonding (π-acidity, especially true for aryl and alkoxy phosphines), and their synthetic accessibility. A possible reason behind this behaviour is the inherent lability of the M–P bond. Phosphine ligands are often easily displaced from the metal centre, and many phosphine-metal complexes show fluxional behaviour in solution.[22,23] In molecular junctions, where molecules are assembled between a pair of metal electrodes, labile phosphine ligands would be driven to coordinate to the electrode rather than to the metal centre, a concept that has been explored in the literature within the principles of the HSAB (Hard–Soft Acid–Base) theory.[24] To our best knowledge, the only reported cases of molecular wires incorporating a metal-phosphine complex are the Co_6Se_8 clusters (and their isostructural derivatives) bearing six phosphine ligands coordinated to the Co centres.[25] In this study, the complex achieves greater stability thanks to π–π interactions between the six ligands, which organise themselves in two π-stacked bundles at opposite sides of the Co_6Se_8 cluster.

Intrigued by these challenges, and driven by the desire to fabricate and characterise well-defined single-molecule junctions based on phosphine-metal complexes, we used the ligand **L** (Fig. 1b) inspired by previous reports of functionalised bis(diphenylphosphino)anilines coordinated to Ag(I) atoms in a linear bis-chelated configuration $[AgL_2]^+$.[26] This molecular arrangement is ideal for our purposes as the linear bis-chelation stabilises the complex (in virtue of the chelating effect) whilst providing a wire-like topology, with the four ancillary phenyl rings offering steric bulk around the metal centre, shielding it from the electrodes. Furthermore, square planar $[PdL_2]^{2+}$ have been shown to link Au-coated microspheres together with much higher efficiency than the ligand **L** alone, with evidence of the complex not decomposing upon exposure to Au surfaces.[27] We therefore used **L** to synthesise three complexes, **1–3** of the type $[M(PNP)_2]PF_6$ (PNP = bis(diphenylphosphino)aniline), with, respectively, Cu(I), Ag(I) and Au(I) centres and hexafluorophosphate (PF_6^-) counterions, and we characterised their interactions with Au with surface-enhanced Raman spectroscopy (SERS) measurements. Their single-molecule conductance was determined with the scanning tunnelling microscope break junction (STMBJ) technique.[28] During our investigation, we found that the three complexes **1–3** are poorly conducting, and that the overall charge transport efficiency is independent of the metal centre. We propose a through-space charge transport mechanism through the complexes that washes out the effect of the metal ion centre, with our hypothesis supported by quantum transport calculations at the density functional theory (DFT) level.

Results and discussion

We synthesised the ligand **L** by treating 4-methylthioaniline with two equivalents of *P*-chlorodiphenylphosphine in the presence of triethylamine as acid scavenger. Complexes **1** and **2** were then prepared by treating the hexafluorophosphate metallic precursor MPF_6 (with M = Cu(I) or Ag(I)) with two equivalents of **L**. The synthesis of **3** was instead achieved by treating two equivalents of ligand **L** with chloro(dimethylsulfide)gold(I), followed by anion metathesis with sodium hexafluorophosphate in a biphasic mixture. All species synthesised were characterised by nuclear magnetic resonance (NMR) and mass spectrometry, and crystals suitable for XRD analysis of **1–3** were obtained by slow vapour diffusion of Et_2O in concentrated solutions of the target compound. The $^{31}P\{^1H\}$ NMR spectra are in all cases consistent with four equivalent phosphorus centres and a tetrahedral coordination environment, with singlets observed at 87.27 and 102.87 ppm, respectively, for **1** and **3**, and well resolved doublets centred at ~97.8 ppm for **2** (Fig. 2a), with coupling constants of $^1J(^{107}Ag,^{31}P)$ = 222 Hz and $^1J(^{109}Ag,^{31}P)$ = 255 Hz, consistent with the literature.[26] The tetrahedral coordination environment is also confirmed by the solid-state structure determined by XRD,[29] however significant distortions are introduced by the small bite angle of the phosphine ligands (see caption of Fig. 2 for selected bond length and angles in **2**, and the SI for similar discussion for **1** and **3**). To the best of our knowledge, this is one of the few examples of tetrahedral Au(I) complexes, complementing those made with other phosphine ligands[30–33] or with the chelating *o*-phenylenebis(dimethylarsine).[34]

We then proceeded at evaluating the stability of the compounds **1–3** on Au by Raman spectroscopy. We employed a Au nanoparticle-based Surface-Enhanced Raman Spectroscopy (SERS) method,[35,36] where Raman-active substrates are fabricated by drop-casting a concentrated solution of Au nanoparticles on a flat Si ⟨100⟩ wafer. The nanoparticles are prepared without a ligand shell and concentrated by centrifugation just before being drop-cast on a Si substrate. A dilute (1 mM) solution of the molecule of interest is then used for adsorption and the Raman laser (785 nm) is focussed on SERS-active areas of the substrate. Further details are available in the methods section, and example results on **1** are reported in Fig. 2c. The Au nanoparticles, with their abundance of undercoordinated Au atoms on their surface, offer similar reactivity to the STMBJ electrodes, and have been used to

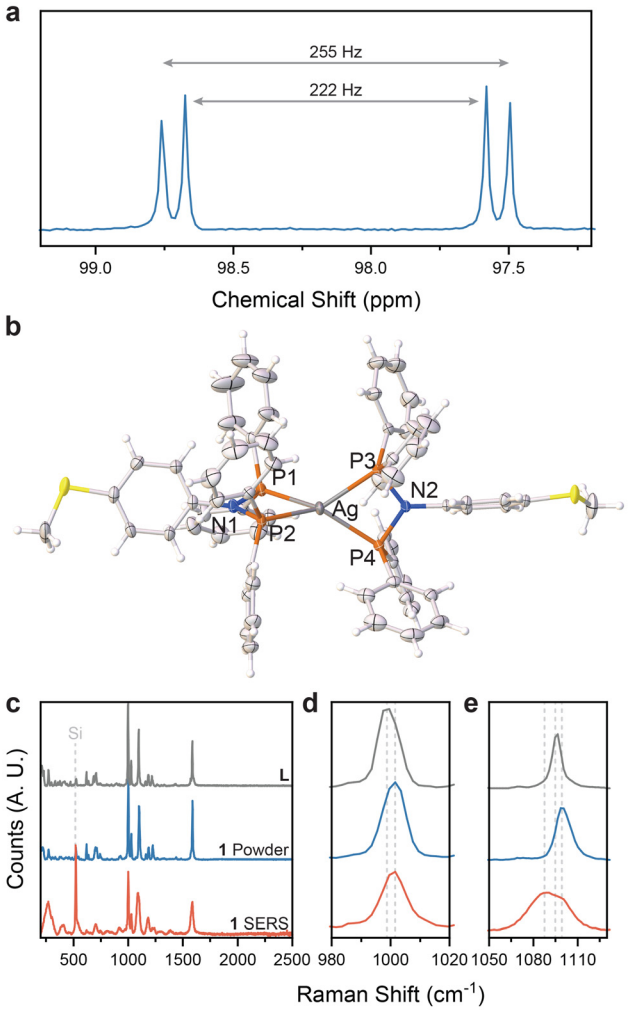

Fig. 2 (a) Expansion of ligand resonances in the $^{31}P\{^{1}H\}$ NMR spectrum for 2 in CD_2Cl_2. (b) ORTEP representation of the molecular structure of 2 (PF_6^- counterion omitted for clarity). Selected bond distances (Å): P1–Ag = 2.548; P2–Ag = 2.455; P3–Ag = 2.495; P4–Ag = 2.501. Selected bond angles (°) = P1–Ag–P2 = 54.083; P3–Ag–P4 = 55.735; P1–Ag–P3 = 128.571; P2–Ag–P4 = 133.103; P1–N1–P2 = 109.756; P3–N2–P4 = 110.223. See ESI† for crystallographic tables. (c) Raman spectra for **L** and **1** (in both powder form and SERS on Au nanoparticles). (d) Magnification of the region 980–1020 cm^{-1} and (e) magnification of the region 1050–1160 cm^{-1}. Colours in (b): C = light grey; H = white; S = yellow; Ag = dark grey, N = blue. Hexafluorophosphate counterions not shown for clarity.

extract information on the molecule–metal interface.[37,38] Comparisons with the Raman spectrum of the sample in its powder form and with the spectrum of the free ligand show that the structure of the molecular wire is retained on Au nanoparticles. For instance, the strong Raman band at ~1000 cm^{-1}, associated with ring breathing, is centred at 998 cm^{-1} in the free ligand, but shifted to 1003 cm^{-1} in the complex, with the same shift occurring in the powdered and SERS sample (Fig. 2d). Significant shifts are observed between the powdered and the SERS samples in the group at ~1100 cm^{-1}, attributed to the thioanisole *S*-Aryl stretch.[39] In the SERS sample, a visible shoulder is developed at lower wavenumber, which we attribute to the formation of the Au–S interface (Fig. 2e). The strong signal at ~1580 cm^{-1}, instead, is not changed significantly by complexation with metallic ions, but it is significantly broadened in the SERS measurements. This peak can be assigned to the C=C stretching mode, and the broadening in the presence of the nanoparticles is due to Au–π interactions.[40] The Aryl-*S*-CH_3 symmetric (684 cm^{-1}) and asymmetric (706 cm^{-1}) stretch signals[39] also broaden significantly in the SERS spectrum, merging into a single contribution centred at 701 cm^{-1}, supporting the hypothesis of strong Au–S interactions. Unfortunately, we were not able to characterise the Au–S modes as they fall below 400 cm^{-1}, an area where background fluorescence in our measurements made any assignment impossible. Similar results were found for compounds **2** and **3**, and further details about the Raman and SERS experiments can be found in the ESI.†

Having established that **1–3** maintain their structure in the presence of Au and interact with the substrate mainly through their thioether termini, we proceeded to perform STMBJ measurements to determine their single-molecule conductance. The STMBJ technique relies on the use of a sharp Au tip, which is driven/crashed into the Au substrate by the piezoelectric transducer of a scanning tunnelling microscope to form a bulk microcontact under electrical bias (300–500 mV in this study). The tip is then slowly withdrawn (10 nm s^{-1} in this study) and as a result the microcontact is stretched and thinned to an atomic point contact, having conductance $G = G_0 = \frac{2e^2}{h} \cong 77.48\,\mu S$, where G_0 is the quantum of conductance (conductance of a fully opened quantum channel). Further withdrawal ruptures the point contact, leaving two atomically sharp nanoelectrodes separated by a small nanogap. When the experiment is performed in the presence of molecules with appropriate binding groups such as the methyl thioethers of **1–3**, these can coordinate to the Au electrodes to bridge the nanogap and assemble a single-molecule junction. The tip withdrawal is continued to stretch the junction to its maximum elongation, until a final rupture. Current through the junction and applied bias are continuously recorded at high sampling speed (20 kHz) by a sensitive transimpedance amplifier and conductance is calculated as $G = I/V$ as a function of the quantum of conductance G_0. This process of crash/withdrawal is repeated thousands of times to acquire statistically significant data. A brief description of the equipment used and the data acquisition and analysis protocols can be found in the ESI,† and more details can be found in our recent publications on the subject.[41,42]

Results of our STMBJ investigation can be found in Fig. 3. No significant differences in charge transport efficiency were found, with all the three complexes studied here showing highly sloped traces and similar features in the STMBJ conductance histograms (see Fig. 3a for individual break-junction traces, and Fig. 3b for the resulting histograms). In all three cases, fabricated junctions are low in conductance ($G \cong 10^{-5}\ G_0$), and they can be extended to lengths only slightly

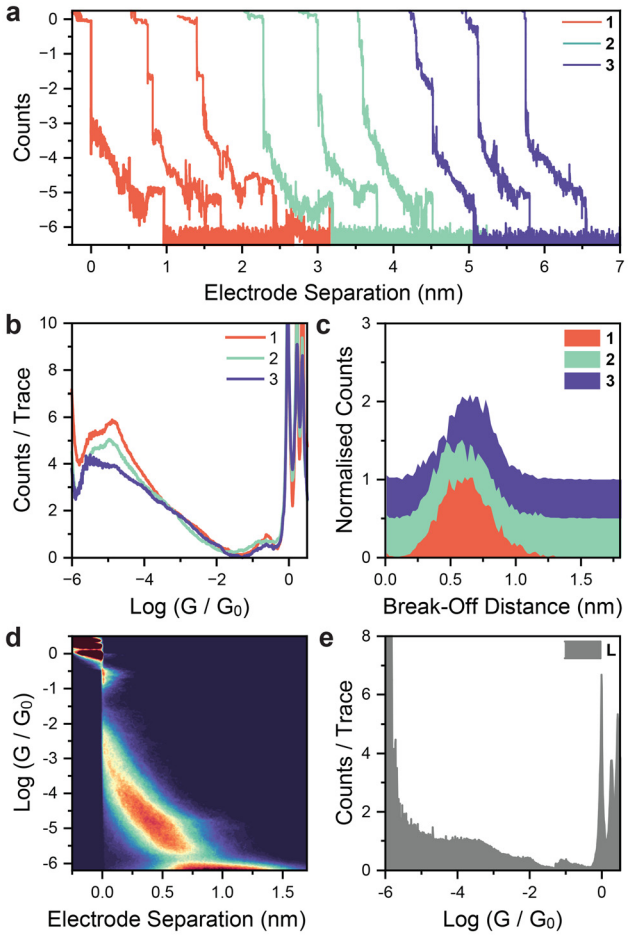

Fig. 3 STMBJ Experiments. (a) Example STMBJ traces for the compounds used in this study. Traces are shifted in 0.75 nm increments for clarity. (b) Comparison of the STMBJ histograms for **1**–**3**, and (c) resulting break-off analysis, not accounting for the electrode snapback. Plots are normalised to the number of traces used and shifted on the *y* axis for clarity. 95th percentile of junction stretching is **1** = 1.10 nm; **2** = 1.14 nm; **3** = 1.15 nm. (d) 2D conductance – electrode separation heatmap for **1**, with the high-intensity area arising from the formation of molecular junctions highlighted. (e) Conductance histogram for the free ligand **L**. All experiments performed in mesitylene, at 500 mV bias. Further experiments at lower bias are reported in the ESI.†

shorter than the S–S distance (~1.8 nm from crystallographic data), considering the 95th percentile of junction stretching[43] calculated from the break-off distance distributions (Fig. 3c, see figure caption for values). Accounting for an electrode snapback values of 0.65 nm as previously reported for mesitylene,[44] we have junctions of length ~1.75, ~1.79 and ~1.80 nm, respectively, for **1**, **2**, and **3** – thus supporting the hypothesis that these compounds do not decompose in the presence of the metallic electrodes, and the fabricated junctions reach, at full extension, the configuration shown in Fig. 1a. The 2D conductance heatmaps (see Fig. 3d for **1** and the ESI† for **2**–**3**) show a quasi-monotonous decay of conductance until break-off, consistent with a junction evolution where the electrodes interact with the ancillary phenyl rings at short electrode separation before finally reaching the fully-extended configuration just before rupture. Such phenomena also explain the shape of the 1D histogram peak, which resembles the envelope of two Gaussian distributions for all three compounds used in this study. As control experiment, we also performed STMBJ experiments on the free ligand **L**, as diphenyl phosphines have been proposed as contact groups in the literature.[45] No distinct conductance peak was resolved in the 1D histogram (Fig. 3e).

To rationalise our results, we performed density functional theory (DFT) calculations on the compounds with different metal centres. We first performed geometry optimisation of molecules in gas phase and between Au electrodes to find the ground state geometry and calculate the mean-field Hamiltonian of the junctions, using the *SIESTA*[46] implementation of DFT. We then combined the obtained Hamiltonian and overlap matrices with the quantum transport code, *GOLLUM*[47] to calculate the transmission probability $T(E)$ of electrons with energy E traversing from one electrode to the other (see Methods for details). The electrical conductance is then obtained from the thermal average of transmission functions from the Landauer Formula. At low temperatures, the conductance $G = G_0T(E_F)$ where G_0 is the conductance quantum and E_F is the Fermi energy of the electrodes.[48]

Transmission calculations at the DFT level support the experimental findings of these compounds having essentially the same charge transport efficiency. Fig. 4 shows the calculated DFT $T(E)$ of the compounds with different metal centres: Cu(I), Ag(I), and Au(I). The transport gap between resonances due to the HOMO and LUMO levels changes slightly between the metal centres. The smallest and largest energy gaps are for compounds **1** and **3**, respectively. As a result, the magnitude of $T(E)$ changes between the HOMO–LUMO gap. For a wide energy range ($E \in [-1.5,0]$ eV, representative of the wide range of electrode structures likely fabricated during the STMBJ measurements), the transmission follows the order **3** > **1** ≥ **2**, but despite the relatively significant HOMO–LUMO gap variations, the effective changes in the transmission amplitudes around E_F are quite small, and the mid-gap region remains

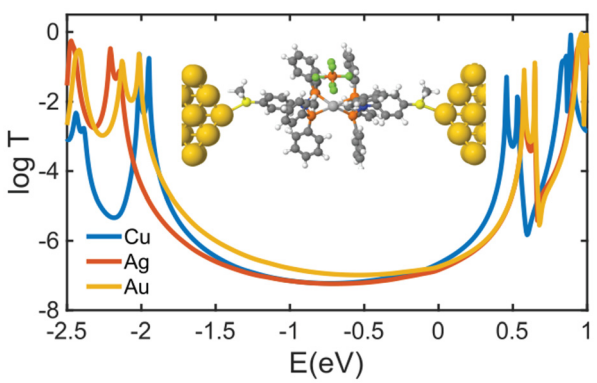

Fig. 4 DFT Transmission coefficient of the compounds with different metal centres. E = 0 eV denotes the DFT-calculated Fermi energy.

featureless. These small changes are averaged out during an STMBJ experiment by sampling range of different electrode structures and interfacial arrangement in each indentation/withdrawal cycle (each with a slightly different value of E_F).

Conclusions

We synthesised molecular wires incorporating two chelating diphosphinoaniline ligands to a monovalent ion of Ag, Au or Cu. The solid-state structure determined by single-crystal XRD of the Au(I) complex showed a distorted tetrahedral geometry. The complexes were characterised by SERS in the presence of Au nanoparticles, highlighting their good stability in the presence of metallic Au and evidence of strong interfacial binding through the aurophilic 4-thioanisolyl termini. Their single-molecule conductance values, measured using the STMBJ technique, were similar with features consistently centred at approximately $10^{-5}G_0$ despite the exchange of the metal centres. These results pave the way for more studies on phosphine-metal-phosphine molecular wires by showing a level of stability sufficient to allow the fabrication of single-molecule electronic devices.

Methods

Synthesis

Reagents were purchased from Sigma-Aldrich, TCI or Fluorochem and they were used without any further purification. All solvents were purchased from ThermoFisher scientific and purified using an Innovative Technology Puresolv system. Ultrapure water was produced by a Merck Direct-Q 3UV and tested to a resistance >18 MΩ before use. NMR spectra were recorded on a Bruker Avance III HD spectrometer. Chemical shifts δ are reported in ppm, referenced against the residual solvent and internal standards. Mass spectrometry was carried out on an Agilent 6540A in ESI mode. Elemental analysis was performed on an Elemental Vario MicroCube. All manipulations were performed in inert atmosphere, using Schlenk techniques.

Synthesis of L

4-Methylthioaniline (1 eq., 15 mmol, 2.1 g, 1.9 mL) and anhydrous triethylamine (2.5 eq., 37.5 mmol, 3.79 g, 5.2 mL) were added to 50 mL of anhydrous tetrahydrofuran under a N_2 atmosphere. Chlorodiphenylphosphine (2 eq., 30 mmol, 6.6 g, 5.5 mL) was then added dropwise. A white precipitate immediately formed, and the suspension was left stirring overnight at room temperature. The white precipitate was then filtered and the residue was washed with 20 mL of anhydrous tetrahydrofuran. The filtrate was collected, and the solvent was evaporated *in vacuo*. Methanol (50 mL) was added, and a white precipitate formed after a brief sonication. The resulting suspension was filtered and the residue was washed with methanol. The residue was purified by recrystallisation (vapour diffusion of hexane into CH_2Cl_2), yielding the title product as white crystals suitable for XRD (6.6 g, 85%). ^{1}H NMR (500 MHz, CD_2Cl_2) δ = 7.36–7.28 (m, 20 H), 6.84–6.82 (d, J = 10 Hz, 2 H), 6.55–6.54 (d, J = 10 Hz, 2 H), 2.35 (s, 3H); ^{13}C{^{1}H} NMR (126 MHz, CD_2Cl_2) δ = 144.96 (s), 139.57–139.46 (t, J = 7.5 Hz), 135.47 (s), 133.71–133.53 (t, J = 11.3 Hz), 129.94–129.89 (t, J = 2.5 Hz), 129.49 (s), 128.46–128.41 (t, J = 2.5 Hz), 126.73 (s), 16.31 (s); ^{31}P{^{1}H} NMR (202 MHz, CD_2Cl_2) δ 67.86 (s). All spectroscopic data are in agreement with the literature.[26]

Synthesis of 1

Tetrakis(acetonitrile)copper(I) hexafluorophosphate (1 eq., 0.15 mmol, 55.93 mg) and ligand **L** (2 eq., 0.3 mmol, 152.42 mg) were dissolved in 4 mL dry DCM. The solution was stirred at room temperature under nitrogen for 2 hours. The solvent was reduced *in vacuo* and the product was precipitated by adding diethyl ether in excess. The white solid was filtered and washed with further diethyl ether to yield the title compound as a white solid (147.95 mg, 0.12 mmol, 80.6%). Found: C = 60.95, H = 4.47, N = 2.17 and S = 5.35%. $C_{62}H_{54}F_6P_5N_2S_2Cu$ requires C = 60.86, H = 4.45, N = 2.29 and S = 5.24% ^{1}H NMR (500 MHz, CD_2Cl_2) δ = 7.52–7.49 (t, J = 7.5 Hz, 8 H), 7.31–7.28 (t, J = 7.5 Hz, 16 H), 7.25–7.23 (m, 16 H), 6.77–6.75 (d, J = 10 Hz, 4 H), 6.22–6.20 (d, J = 10 Hz, 4 H), 2.32 (s, 6 H). ^{13}C{^{1}H} NMR (125.721 MHz, CD_2Cl) δ = 139.33 (s), 136.19 (s), 133.39–133.24 (p, J = 5.0 Hz), 133.05–132.76 (p, J = 8.8 Hz), 132.18 (s), 130.39 (s), 129.59–129.51 (t, J = 5.0 Hz), 126.08 (s), 15.32 (s). DEPT-135 (125.721 MHz, CD_2Cl_2) δ = 132.97–132.82 (p, J = 5.0 Hz), 131.76 (s), 129.97 (s), 129.17–129.09 (t, J = 5.0 Hz), 125.66 (s), 14.89 (s). ^{31}P{^{1}H} NMR (202.404 MHz, CD_2Cl_2) δ = 87.27 (s), −135.33–156.38 (PF_6 hept, J = 708 Hz). m/z (HRMS, ESI) 1077.2079 $[M]^+$, $[C_{62}H_{54}P_4N_2S_2Cu]^+$ calc. 1077.19694.

Synthesis of 2

Ligand **L** (415.58 mg, 0.80 mmol, 2 eq.) and silver(I) hexafluorophosphate (103.48 mg, 0.40 mmol, 1 eq.) were dissolved in 40 mL of dry acetone. The solution was stirred at room temperature under nitrogen in the absence of light for 4 hours. The solvent was reduced *in vacuo* and the product was precipitated by addition of an excess of *n*-pentane. The resulting white solid was filtered, washed by further *n*-pentane and collected (297.24 mg, 0.23 mmol, 57.3%). Found: C = 58.99, H = 4.36, N = 2.21 and S = 5.06%. $C_{62}H_{54}F_6P_5N_2S_2Ag$ requires C = 58.73, H = 4.29, N = 2.21 and S = 5.06%. ^{1}H NMR (500 MHz, CD_2Cl_2) δ = 7.52–7.49 (t, J = 7.5 Hz, 8 H), 7.35–7.32 (m, 32 H), 6.75–6.73 (d, J = 10 Hz, 4 H), 6.11–6.09 (d, J = 10 Hz, 4 H), 2.33 (s, 6 H). ^{13}C{^{1}H} NMR (125.721 MHz, CD_2Cl) δ = 139.32 (s), 136.84 (s), 133.59–133.43 (t, J = 10 Hz), 133.08 (s), 132.14 (s), 130.74 (s), 129.51 (s), 125.89 (s), 15.34 (s). DEPT-135 (125.721 MHz, CD_2Cl_2) δ = 133.18–133.01 (t, J = 10.7 Hz), 131.72 (s), 130.33 (s), 129.10 (s), 125.48 (s), 14.93 (s). ^{31}P{^{1}H} NMR (202.404 MHz, CD_2Cl_2) δ = 98.75–97.50 (dd, $J(^{109}Ag/P)$ = 253 Hz, $J(^{107}Ag/P)$ = 221 Hz), −134.01–155.06 (PF_6 hept, J = 710 Hz). m/z (HRMS, ESI) 1121.1732 $[M]^+$, $[C_{62}H_{54}P_4N_2S_2Ag]^+$ calc. 1121.17243.

Synthesis of 3

Ligand **L** (345.96 mg, 0.68 mmol, 2 eq.) and dimethylsulfide gold(I) chloride (100.13 mg, 0.34 mmol, 1 eq.) were dissolved in 20 mL dry dichloromethane, and the solution was stirred at room temperature under nitrogen for 90 minutes. After this time, 10 mL of 1 M sodium hexaflurophosphate solution in deionized water was injected in the reaction flask and the biphasic mixture was vigorously stirred for 1 hour. The organic phase was extracted with dichloromethane, separated, and dried with anhydrous magnesium sulphate. The filtrate was reduced *in vacuo* and diethyl ether was added to precipitate the title product as an off-white solid (345.32 mg, 0.25 mmol, 74.9%). Found: C = 54.18, H = 4.05, N = 1.99 and S = 4.86%. $C_{62}H_{54}F_6P_5N_2S_2Au$ requires C = 54.87, H = 4.01, N = 2.06 and S = 4.72%. ^{1}H-NMR (500 MHz, CD_2Cl_2) δ = 7.53–7.49 (m, 8H), 7.32–7.31 (m, 32 H), 6.78–6.76 (d, J = 10 Hz, 4 H), 6.23–6.21 (d, J = 10 Hz, 4 H), 2.33 (s, 6 H). ^{13}C{^{1}H} NMR (125.721 MHz, CD_2Cl) δ = 139.63 (s), 137.81 (s), 133.53–133.37 (p, J = 5.0 Hz), 132.77 (s), 132.31 (s), 130.66 (s), 129.46–129.38 (t, J = 5.0 Hz), 126.06 (s), 15.29 (s). DEPT-135 (125.721 MHz, CD_2Cl_2) δ = 133.11–132.95 (p, J = 5.0 Hz), 131.89 (s), 130.24 (s), 129.04–128.96 (t, J = 5.0 Hz), 125.64 (s), 14.87 (s). ^{31}P{^{1}H} NMR (202.404 MHz, CD_2Cl_2) δ = 102.87 (s), −134.00–155.05 (PF_6 hept, J = 710 Hz). m/z (HRMS, ESI) 1211.23391 $[M]^+$, $[C_{62}H_{54}P_4N_2S_2Au]^+$ calc. 1211.23391.

X-ray diffraction

X-ray quality crystals of the three complexes **1–3** were grown by diffusion of diethyl ether in concentrated dichloromethane solutions of the desired compound. See ESI† for specific detail on data acquisition, processing, and crystallographic tables.

Single-molecule conductance measurements

We used a modified Keysight Technology 5500 STM for all measurements. Details of the modifications we performed to the commercial instrument are reported in our previous publications,[42,49] and a brief description and schematics are provided in the ESI,† along with further information about the materials and parameters used in our experiments.

Raman spectroscopy and SERS

We used a Metrohm/B&W Tek MiniRam instrument, equipped with a 785 nm diode laser. Powder Raman spectra were acquired directly from the samples. We synthesised nanoparticles for SERS following a published procedure[50] that gives ~55 nm diameter particles. In brief, 100 mL of 0.01 wt% solution of chloroauric acid trihydrate is brought to reflux, and 0.7 mL of sodium citrate is added in a single portion. The solution is left boiling for 30 minutes, followed by cooling to room temperature. 50 mL aliquots of the resulting nanoparticle colloidal suspension are then centrifuged (99 minutes, 4000 rpm) to concentrate the nanoparticles. The clear supernatant is carefully removed, resulting in final volumes of ~0.5 mL per 50 mL aliquot of mother solution. The concentrated nanoparticle suspensions, deep purple in colour, are then drop-casted on clean Si wafers, which are then dried in vacuum overnight to deliver SERS substrates. Molecular adsorption is achieved by immersion of the substrates in dilute (1 mM) solutions of the molecule of interest, followed by a gentle rinse with pure solvent, and dried under a stream of N_2 before use in the spectrometer.

Density functional theory calculations

The geometry of each structure studied in this paper was relaxed to the force tolerance of 10 meV Å^{-1} using the *SIESTA*[46] implementation of DFT, with a double-ζ polarized basis set (DZP) and the Generalized Gradient Approximation (GGA) functional with Perdew–Burke–Ernzerhof (PBE) parametrization. A real-space grid was defined with an equivalent energy cutoff of 250 Ry.

Quantum transport

To calculate the electronic properties of the device from the converged DFT calculation, the underlying mean-field Hamiltonian H was obtained. H was combined with the quantum transport code *GOLLUM*.[47] This yields the transmission coefficient $T(E)$ for electrons of energy E (passing from the source to the drain) *via* the relation $T(E) = \mathrm{Tr}(\Gamma_L(E) G_\sigma(E)\Gamma_R(E)G_\sigma^\dagger(E))$, where $\Gamma_{L,R}(E) = i\left(\sum_{L,R}(E) - \sum_{L,R}^\dagger(E)\right)$ describes the level broadening due to the coupling between left L and right R electrodes and the central scattering region, $\Sigma_{L,R}(E)$ is the retarded self-energy associated with this coupling, and $G^R = (ES - H - \Sigma_L - \Sigma_R)^{-1}$ is the retarded Green's function, where H is the Hamiltonian and S is the overlap matrix obtained from the *SIESTA* implementation of DFT. The room temperature electrical conductance then can be calculated from the Landauer formula.

Data availability

All raw data supporting this work and bespoke software used for data processing are available online on the University of Liverpool Data Catalogue at **https://doi.org/10.17638/datacat.liverpool.ac.uk/2469** (original submission) and **https://doi.org/10.17638/datacat.liverpool.ac.uk/2965** (manuscript revision). Crystal structure data are available in the Cambridge Structural Database under deposition number CCDC 2408349–2408351.†

Author contributions

MFG: investigation, data curation, formal analysis, writing – original draft. SS: investigation, data curation, formal analysis, writing – original draft. DJ: investigation, data curation. EB: investigation. AS: data curation, formal analysis, supervision. GAK: supervision, funding acquisition. SJH: supervision, formal analysis. CMR: investigation, data curation, formal analysis. RJN: supervision, resources, methodology. HS: supervision, funding acquisition, resources, software. AV: conceptualisation, resources, project administration, funding acquisition,

software, methodology, formal analysis, writing – original draft. All authors contributed to reviewing and editing this document.

Conflicts of interest

There are no conflicts to declare.

Acknowledgements

This work was primarily supported by the Royal Society (URF \R1\191241 and RGS\R2\202119), and A. V. also acknowledges generous support from EPSRC (EP/V037765/1). H. S. thanks UKRI for a Future Leaders Fellowship (MR/S015329/2 and MR/X015181/1). S. S. acknowledges the Leverhulme Trust for an Early Career Fellowship (ECF-2018-375). D. J. acknowledge the Australian Government for a RTP stipend and the Royal Society of Chemistry for a Researcher Collaboration Grant.

References

1 A. Vezzoli, *Encycl. Inorg. Bioinorg. Chem*, Wiley, 2021.
2 X. Xiao, D. Brune, J. He, S. Lindsay, C. B. Gorman and N. Tao, *Chem. Phys.*, 2006, **326**, 138–143.
3 Y. Li, H. Wang, Z. Wang, Y. Qiao, J. Ulstrup, H.-Y. Chen, G. Zhou and N. Tao, *Proc. Natl. Acad. Sci. U. S. A.*, 2019, **116**, 3407–3412.
4 T. C. Ting, L. Y. Hsu, M. J. Huang, E. C. Horng, H. C. Lu, C. H. Hsu, C. H. Jiang, B. Y. Jin, S. M. Peng and C. H. Chen, *Angew. Chem., Int. Ed.*, 2015, **54**, 15734–15738.
5 P. J. Chen, M. Sigrist, E. C. Horng, G. M. Lin, G. H. Lee, C. H. Chen and S. M. Peng, *Chem. Commun.*, 2017, **53**, 4673–4676.
6 R. Frisenda, G. D. Harzmann, J. A. Celis Gil, J. M. Thijssen, M. Mayor and H. S. J. van der Zant, *Nano Lett.*, 2016, **16**, 4733–4737.
7 M. Camarasa-Gómez, D. Hernangómez-Pérez, M. S. Inkpen, G. Lovat, E.-D. Fung, X. Roy, L. Venkataraman and F. Evers, *Nano Lett.*, 2020, **20**, 6381–6386.
8 D. C. Milan, A. Vezzoli, I. J. Planje and P. J. Low, *Dalton Trans.*, 2018, **47**, 14125–14138.
9 Y. Tanaka, Y. Kato, T. Tada, S. Fujii, M. Kiguchi and M. Akita, *J. Am. Chem. Soc.*, 2018, **140**, 10080–10084.
10 S. Chappell, C. Brooke, R. J. Nichols, L. J. Kershaw Cook, M. Halcrow, J. Ulstrup and S. J. Higgins, *Faraday Discuss.*, 2016, **193**, 113–131.
11 X. S. Zhou, L. Liu, P. Fortgang, A. S. Lefevre, A. Serra-Muns, N. Raouafi, C. Amatore, B. W. Mao, E. Maisonhaute and B. Schöllhorn, *J. Am. Chem. Soc.*, 2011, **133**, 7509–7516.
12 J. Ponce, C. R. Arroyo, S. Tatay, R. Frisenda, P. Gaviña, D. Aravena, E. Ruiz, H. S. J. van der Zant and E. Coronado, *J. Am. Chem. Soc.*, 2014, **136**, 8314–8322.
13 E. Koyama, Y. Naitoh, H. Tokuhisa, T. Nakamura, M. Horikawa, T. Ishida, K. Fujiwara, W. Mizutani, Y. Nagawa and M. Kanesato, *Jpn. J. Appl. Phys.*, 2008, **47**, 7369–7371.
14 Y. Lee, S. Yuan, A. Sanchez and L. Yu, *Chem. Commun.*, 2008, **1**, 247–249.
15 Y. Lee, S. Yuan and L. Yu, *Sci. China: Chem.*, 2011, **54**, 410–414.
16 J. Park, A. N. Pasupathy, J. I. Goldsmith, C. Chang, Y. Yaish, J. R. Petta, M. Rinkoski, J. P. Sethna, H. D. Abruña, P. L. McEuen and D. C. Ralph, *Nature*, 2002, **417**, 722–725.
17 N. Tuccitto, V. Ferri, M. Cavazzini, S. Quici, G. Zhavnerko, A. Licciardello and M. A. Rampi, *Nat. Mater.*, 2009, **8**, 41–46.
18 M. Ruben, A. Landa, E. Lörtscher, H. Riel, M. Mayor, H. Görls, H. B. Weber, A. Arnold and F. Evers, *Small*, 2008, **4**, 2229–2235.
19 Y. Cao, S. Dong, S. Liu, L. He, L. Gan, X. Yu, M. L. Steigerwald, X. Wu, Z. Liu and X. Guo, *Angew. Chem., Int. Ed.*, 2012, **51**, 12228–12232.
20 M. Meng, Z. Tang, S. Mallick, M. H. Luo, Z. Tan, J. Y. Liu, J. Shi, Y. Yang, C. Y. Liu and W. Hong, *Nanoscale*, 2020, **12**, 10320–10327.
21 N. Cheng, L. Zhang, C. Durkan, N. Wang, B. Du, J. Zhao and Y. He, *J. Phys. Chem. C*, 2020, **124**, 21137–21146.
22 Y. Otero, D. Peña, A. Arce, M. Hissler, R. Réau, Y. De Sanctis, E. Ocando-Mavárez, R. Machado and T. González, *J. Organomet. Chem.*, 2015, **799–800**, 45–53.
23 N. K. Kiriakidou Kazemifar, M. J. Stchedroff, M. A. Mottalib, S. Selva, M. Monari and E. Nordlander, *Eur. J. Inorg. Chem.*, 2006, **2006**, 2058–2068.
24 H. E. Skipper, C. V. May, A. L. Rheingold, L. H. Doerrer and M. Kamenetska, *J. Am. Chem. Soc.*, 2021, **143**, 16439–16447.
25 B. Choi, B. Capozzi, S. Ahn, A. Turkiewicz, G. Lovat, C. Nuckolls, M. L. Steigerwald, L. Venkataraman and X. Roy, *Chem. Sci.*, 2016, **5**, 476–482.
26 A. Ghisolfi, C. Fliedel, P. de Frémont and P. Braunstein, *Dalton Trans.*, 2017, **46**, 5571–5586.
27 C. Fliedel, V. Faramarzi, V. Rosa, B. Doudin and P. Braunstein, *Chem. – Eur. J.*, 2014, **20**, 1263–1266.
28 B. Xu and N. Tao, *Science*, 2003, **301**, 1221–1223.
29 R. Ahuja, M. Nethaji and A. G. Samuelson, *Inorg. Chim. Acta*, 2011, **372**, 220–226.
30 R. C. Elder, E. H. K. Zeiher, M. Onady and R. R. Whittle, *J. Chem. Soc., Chem. Commun.*, 1981, 900–901.
31 S. J. Berners-Price and P. J. Sadler, *Inorg. Chem.*, 1986, **25**, 3822–3827.
32 M. Osawa, I. Kawata, S. Igawa, M. Hoshino, T. Fukunaga and D. Hashizume, *Chem. – Eur. J.*, 2010, **16**, 12114–12126.
33 P. A. Bates and J. M. Waters, *Inorg. Chim. Acta*, 1984, **81**, 151–156.
34 R. Usón, A. Laguna, J. Vicente, J. Garcia, P. G. Jones and G. M. Sheldrick, *J. Chem. Soc., Dalton Trans.*, 1981, 655–657.
35 F. Tian, F. Bonnier, A. Casey, A. E. Shanahan and H. J. Byrne, *Anal. Methods*, 2014, **6**, 9116–9123.

36 J. Ward, A. Vezzoli, C. Wells, S. Bailey, S. P. Jarvis, C. J. Lambert, C. Robertson, R. Nichols and S. Higgins, *Angew. Chem., Int. Ed.*, 2024, **63**, e202403577.
37 J. Liang, R. E. G. Smith, A. Vezzoli, L. Xie, D. C. Milan, R. Davidson, A. Beeby, P. J. Low, S. J. Higgins, B. Mao and R. J. Nichols, *Electrochim. Acta*, 2016, **220**, 436–443.
38 I. L. Herrer, A. K. Ismael, D. C. Milán, A. Vezzoli, S. Martín, A. González-Orive, I. Grace, C. Lambert, J. L. Serrano, R. J. Nichols and P. Cea, *J. Phys. Chem. Lett.*, 2018, **9**, 5364–5372.
39 M.-X. Liu, B.-B. Xie, M.-J. Li, Y.-Y. Zhao, K.-M. Pei, H.-G. Wang and X. Zheng, *J. Raman Spectrosc.*, 2013, **44**, 440–446.
40 R. Tandiana, C. Sicard-Roselli, N.-T. Van-Oanh, S. Steinmann and C. Clavaguéra, *Phys. Chem. Chem. Phys.*, 2022, **24**, 25327–25336.
41 A. Daaoub, J. M. F. Morris, V. A. Béland, P. Demay-Drouhard, A. Hussein, S. J. Higgins, H. Sadeghi, R. J. Nichols, A. Vezzoli, T. Baumgartner and S. Sangtarash, *Angew. Chem., Int. Ed.*, 2023, **62**, e202302150.
42 S. Naghibi, S. Sangtarash, V. J. Kumar, J.-Z. Wu, M. M. Judd, X. Qiao, E. Gorenskaia, S. J. Higgins, N. Cox, R. J. Nichols, H. Sadeghi, P. J. Low and A. Vezzoli, *Angew. Chem., Int. Ed.*, 2022, **61**, e202116985.
43 B. Capozzi, E. J. Dell, T. C. Berkelbach, D. R. Reichman, L. Venkataraman and L. M. Campos, *J. Am. Chem. Soc.*, 2014, **136**, 10486–10492.
44 S. Y. Quek, M. Kamenetska, M. L. Steigerwald, H. J. Choi, S. G. Louie, M. S. Hybertsen, J. B. Neaton and L. Venkataraman, *Nat. Nanotechnol.*, 2009, **4**, 230–234.
45 R. Parameswaran, J. R. Widawsky, H. Vázquez, Y. S. Park, B. M. Boardman, C. Nuckolls, M. L. Steigerwald, M. S. Hybertsen and L. Venkataraman, *J. Phys. Chem. Lett.*, 2010, **1**, 2114–2119.
46 J. M. Soler, E. Artacho, J. D. Gale, A. García, J. Junquera, P. Ordejón and D. Sánchez-Portal, *J. Phys.: Condens. Matter*, 2002, **14**, 2745–2779.
47 J. Ferrer, C. J. Lambert, V. M. García-Suárez, D. Z. Manrique, D. Visontai, L. Oroszlany, R. Rodríguez-Ferradás, I. Grace, S. W. D. Bailey, K. Gillemot, H. Sadeghi and L. A. Algharagholy, *New J. Phys.*, 2014, **16**, 093029.
48 H. Sadeghi, *Nanotechnology*, 2018, **29**, 373001.
49 C. Wu, X. Qiao, C. M. Robertson, S. J. Higgins, C. Cai, R. J. Nichols and A. Vezzoli, *Angew. Chem., Int. Ed.*, 2020, **59**, 12029–12034.
50 J. F. Li, X. D. Tian, S. B. Li, J. R. Anema, Z. L. Yang, Y. Ding, Y. F. Wu, Y. M. Zeng, Q. Z. Chen, B. Ren, Z. L. Wang and Z. Q. Tian, *Nat. Protoc.*, 2013, **8**, 52–65.